

RESEARCH ARTICLE

10.1029/2017JB014986

Subsurface Structure of Long Valley Caldera Imaged With Seismic Scattering and Intrinsic Attenuation

Key Points:

- Two-dimensional attenuation images over the first 3–5 km below Long Valley Caldera obtained by space-weighted mapping
- Attenuation images identify the shallow hydrothermal system at Long Valley Caldera
- Hartley Springs Fault has different attenuation behavior on each side and may reflect remaining heat produced by Inyo Crater eruptions

Correspondence to:

J. Prudencio,
janire@berkeley.edu

Citation:

Prudencio, J., Manga, M., & Taira, T. (2018). Subsurface structure of Long Valley Caldera imaged with seismic scattering and intrinsic attenuation. *Journal of Geophysical Research: Solid Earth*, 123, 5987–5999. <https://doi.org/10.1029/2017JB014986>

Received 13 SEP 2017

Accepted 19 JUN 2018

Accepted article online 28 JUN 2018

Published online 31 JUL 2018

J. Prudencio^{1,2,3} , M. Manga^{1,2} , and T. Taira² 

¹Department of Earth and Planetary Science, University of California, Berkeley, CA, USA, ²Berkeley Seismological Laboratory, University of California, Berkeley, CA, USA, ³Andalusian Institute of Geophysics, University of Granada, Granada, Spain

Abstract We image seismic intrinsic (Q_i^{-1}) and scattering (Q_s^{-1}) attenuations in Long Valley Caldera, California, by analyzing more than 1,700 vertical component waveforms from local earthquakes. Observed energy envelopes are fit to the diffusion model and seismic attenuation images are produced using two-dimensional space weighting functions. Low intrinsic and low scattering attenuation anomalies in the center south of the caldera correspond to the location of an earthquake swarm in 2014. We identify high intrinsic and high scattering attenuation anomalies in the fluid-rich western and eastern areas of the caldera. From a comparison with other geophysical images (magnetotellurics and seismic tomography) we attribute these anomalies to a hydrothermal system (high attenuation). Average to high attenuation values are also observed at the adjacent Mammoth Mountain (southwest of the caldera) and may also have a hydrothermal origin. High intrinsic attenuation at low frequencies to the west of the Hartley Springs Fault may be produced by the magmatic system that produced the Inyo Craters. Seismic attenuation imaging provides insights into subsurface structures that are complementary to velocity and conductivity images.

1. Introduction

Long Valley is an ellipsoidal caldera located in eastern California that formed 756 ka (Bailey et al., 1976). Other major geologic structures in the area include ENE-dipping range-front normal faults, including the Hartley Springs Fault (HSF) north of the caldera and Hilton Creek Fault (HCF) to the south, and Mammoth Mountain, situated outside the southwest edge of the caldera. More recent rhyolitic eruptions within the caldera took place 570–505, 360–330, 150, and 115–110 ka (Heumann et al., 2002). The most recent volcanic activity in the region occurred outside the structural caldera (Hildreth, 2004) in a north-south trending zone that includes Mono-Inyo Craters (35–0.6 ka, rhyolitic), Mammoth Mountain (200–500 ka, basalt through dacite) and eruptions in Mono Lake (250 years old, dacitic). The entire system may be underlain by an elongate feeder system (e.g., Eichelberger et al., 1984; Fink, 1985; Miller, 1985).

Unrest at Long Valley began in 1978 south of the caldera and migrated into the caldera in 1980 (Rundle & Hill, 1988). In 1980 four $M \approx 6$ earthquakes occurred at the edge of the Sierra Nevada block (Taylor & Bryant, 1980). Since then there have been numerous earthquake swarms including a major swarm in 1983 and a long-duration swarm in 1997–1998 (Hill et al., 2003; Prejean et al., 2002). All these swarms were accompanied by rapid uplift of the resurgent dome within the caldera (Dreger et al., 2000; Hill, 2006). The most recent earthquake swarm occurred in 2014 (Shelly et al., 2015). It was the largest swarm in the caldera since the 1997–1998 swarm and occurred below the southeast edge of the resurgent dome. Shelly et al. (2016) attributed the upward migration of hypocenters to rapid ascent of high-pressure low-viscosity aqueous fluids.

Earthquake swarms are also common at adjacent Mammoth Mountain. Upper crustal swarms were reported in 1989 (Hill & Prejean, 2005; Prejean et al., 2003) and 2014 (Shelly et al., 2015). In 1989 an earthquake swarm 6 months in duration was reported along with deformation, long-period events, increased heat flow, and venting of volcanic gases (Hill et al., 1990). These swarms have been attributed to CO_2 -rich fluids, and fluctuations in surface CO_2 emissions are correlated with deeper swarm activity (Lewicki et al., 2014).

Together with earthquake swarms, Long Valley has experienced episodes of uplift centered on the resurgent dome (Langbein, 2003; Savage et al., 1987; Tizzani et al., 2009) and no important subsidence has been

reported. A key question is whether the seismicity and uplift are the result of new injections of magma within the crust or have a hydrological origin.

Based on some combination of deformation and microgravity data, a number of studies have attributed the uplift to magma intrusion (Battaglia, Segall, Murray, et al., 2003; Battaglia, Segall, Roberts, 2003; Langbein, 2003; Montgomery-Brown et al., 2015). A host of tomographic images of the region have been produced over the past decades (e.g., Black et al., 1991; Kissling, 1988; Foulger et al., 2003), and in some images, low velocities are attributed to partial melt (Foulger et al., 2003; Seccia et al., 2011) including at depths as shallow as 5 km (e.g., Lin, 2015). Nakata and Shelly (2018) imaged a reflector at around 8.2 km below the caldera, which they propose to be the upper surface of residual magma. Importantly, detecting melt is a necessary but not sufficient condition for uplift to be promoted by intrusion. While the geodetic and microgravity data document temporal changes, the seismic images provide a static picture and hence cannot address where and when changes occurred.

In contrast, a variety of geological and geochemical measurements suggest that new intrusions are unlikely. There was a great reduction in the intracaldera eruption rate since 650 ka (Hildreth, 2004), there is a modest CO₂ flux on the south flank of the resurgent dome (Bergfeld et al., 2006) that Lucic et al. (2015) found is mainly biogenic, heat flow is normal (Hurwitz et al., 2010), seismicity is low (Hill, 2006; Prejean et al., 2002; Shelly et al., 2016), and low Helium isotope ratios do not indicate new magma (Suemnicht et al., 2015). Instead, a number of studies have proposed that the uplift is produced by the upward migration of aqueous fluids released from old, crystallizing magmas at depth (e.g., Hildreth, 2017; Hurwitz et al., 2007; Hutnak et al., 2009). Cold temperatures (Hurwitz et al., 2010) and hydrothermal mineral deposits (Sorey et al., 1991) in a deep well within the resurgent dome, and an electrically conductive anomaly beneath the dome (Peacock et al., 2016), suggest instead that this region is a fossil hydrothermal system. The seismic swarms (Hill, 2006) and shallow geothermal flows (Hurwitz et al., 2010; Lucic et al., 2015) occur south of this inferred fossil hydrothermal system.

The role of active magmatism beneath Mammoth Mountain is more clear given the combination of large gas emissions (Lewicki et al., 2014) and both shallow and deep seismicity (Shelly & Hill, 2011; Shelly et al., 2015). At Mammoth, electrical resistivity images also identify anomalies that may be produced by active hydrothermal systems (Hill, 1976; Peacock et al., 2016).

Here we use seismic attenuation imaging and its strong relationship to the thermal state of the rocks and the structural complexity of the medium to identify subsurface features (e.g., Del Pezzo, 2008; De Siena et al., 2014; Martínez-Arevalo et al., 2005; Prudencio et al., 2015; Sato et al., 2012). As both types of attenuation (scattering, Q_s^{-1} , structural complexity and intrinsic, Q_i^{-1} , thermal state) may be significant at volcanoes, distinguishing between Q_i^{-1} and Q_s^{-1} may help us interpret subsurface anomalies.

In the present study, we obtain two-dimensional intrinsic (Q_i^{-1}) and scattering (Q_s^{-1}) attenuation images of Long Valley Caldera by applying the fitting procedure described in Wegler and Lühr (2001) with the diffusion model and the back projection technique proposed by Prudencio et al. (2013) and improved by Del Pezzo et al. (2016). We use local earthquakes and stations and hence are able to probe the upper 3–5 km of the crust, limiting our ability to characterize deeper structure. Nevertheless, in combination with geological observations, geochemical measurements, and other geophysical images that are sensitive to other physical parameters, we confirm that seismic attenuation images may identify faults as well as fossil and active hydrothermal systems. We find no evidence for large magma bodies at shallow (3- to 5-km) depths.

2. Methods, Data, and Data Processing

2.1. Data

We analyzed seismic recordings of 3,694 local earthquakes ($M \geq 1.5$) from 2000 through the end of November 2016 identified by the Northern California Seismic System and with focal depths shallower than 10 km (Figure 1). The vertical component seismic recordings for short-period geophones and broadband sensors (a total of 73 sites) were obtained from the Northern California Earthquake Data Center (NCEDC, 2014). The instrument responses were corrected, and a 0.5-Hz high-pass filter was applied to minimize microseism noise.

2.2. Multiple Scattering, the Diffusion Model

Del Pezzo et al. (2006) studied seismic attenuation at Mount Vesuvius using small local volcano-tectonic earthquakes. They fitted more than 400 S-coda envelopes to multiple scattering (following Zeng's approximation,

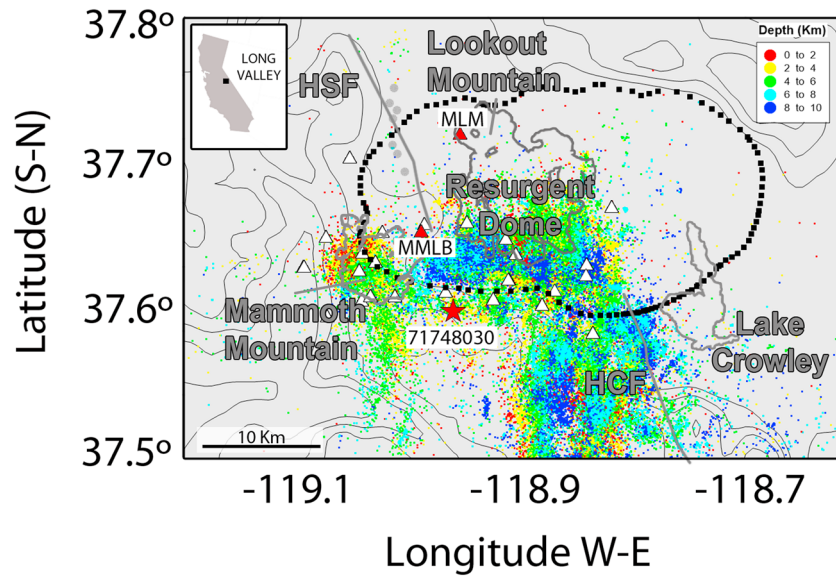


Figure 1. Topographic map of Long Valley Caldera where the boundary of the caldera is marked with black squares. Earthquakes (colored dots) and stations (white triangles) used in the analysis are also shown. The red star with its label (71748030) and two station labeled (red triangles, MLM and MMLB) correspond to the examples of Figure 2. Bigger gray dots correspond to Inyo Crater vents. The box in the insert map shows the location of Long Valley Caldera in California. HSF = Hartley Springs Fault.

Zeng, 1991) and diffusion models to separately obtain intrinsic and scattering quality factors. They concluded that the multiple scattering and diffusion models produce similar results, which suggests that the diffusion regime can be assumed to describe the seismic energy decay. For the diffusion model to be valid, the lapse time, t , should be greater than the transport mean free path, l_{tr} , divided for the wave velocity:

$$t > l_{tr}/v \quad (1)$$

As shown in the results section, this condition is fulfilled at Long Valley and, therefore, we assumed that diffusion model is an appropriate approximation for the region.

We applied the transport equation in its asymptotic approximation (diffusion model) to separately determine scattering and intrinsic attenuation coefficients (Sato et al., 2012). We followed the fitting procedure described by Wegler and Lühr (2001) that was used to model seismic attenuation at Merapi volcano.

2.3. Data Processing

The seismogram energy envelope is described by a diffusion model, $E[r, t]$, as a function of source-receiver distance, r , and time since origin, t ,

$$E[r, t] = E_0(4\pi dt)^{-p/2} \exp \left[-\frac{r^2}{4dt} - bt \right] \quad (2)$$

where E_0 is the energy at the source, d is the diffusivity, b is the intrinsic attenuation coefficient, and p represents the geometrical spreading term (Dainty & Toksöz, 1981). Attenuation coefficients d and b are directly related to intrinsic and scattering quality factors, Q_i and Q_s , respectively, through the following equations:

$$Q_i = \frac{2\pi f}{b} \quad (3)$$

$$Q_s = \frac{2\pi f p d}{v^2} \quad (4)$$

where f is the central frequency of filtered seismograms and v is the half-space velocity. We used a constant velocity of $v = 3.4$ km/s, which is the average S -wave velocity from the P -wave velocity model by Lin (2015)

assuming a V_p/V_s ratio of 1.7. As scattered waves composing the coda in volcanic regions propagate mostly in the uppermost crust (Del Pezzo et al., 1997), we considered only the first 5 km to average the velocity. Finally, total Q can be defined by

$$Q_t^{-1} = Q_i^{-1} + Q_s^{-1} \quad (5)$$

For each seismogram intrinsic and scattering coefficients were estimated by the following procedure:

1. **Filtering.** We carried out a spectral analysis to select the central frequency bands to filter the seismograms. Based on this analysis, seismic signals were filtered at seven frequency bands using Butterworth band-pass filters of eight poles with corner frequencies at $0.4f_c$ and $1.6f_c$ (bandwidth of $f_c \pm 0.6f_c$). The central frequencies, f_c , of selected frequency bands are 4, 6, 8, 12, 16, 20, and 24 Hz. Signal-to-noise ratio was measured in each seismogram, and all the waveforms with a value lower than 2 were rejected. The final data set contains more than 1,700 vertical waveforms for the lowest frequency (4 Hz) and up to 22,000 for highest frequency (24 Hz). Figure 2a shows two examples of filtered seismograms and the corresponding unfiltered signal's spectrum.
2. **Signal extraction.** We extracted filtered seismograms from the S wave onset to 30 s measured from the origin time. Hence, t_{\min} is equal to S -wave arrival time and t_{\max} corresponds to the time interval, which is always 30 s. Figure 2b shows the selected signal window.
3. **Signal envelope.** Energy envelopes of the seismograms were obtained by applying a Hilbert transform to 1.4-s moving windows with an overlap of 50% to the neighboring window for each frequency band.
4. **Parameter estimation.** We fit energy envelopes to equation (2) by using a least square method to obtain b and d and, consequently, Q_i and Q_s . The first term of equation (2), $E_0(4\pi dt)^{-p/2}$, is also obtained from the fit and has no influence on the waveform but only on the absolute value, and therefore, it is not used to estimate attenuation values. The trade-off between b and d parameters was analyzed in Prudencio et al. (2013). They obtained an uncertainty interval of 8% and 6% for b and d , respectively. The lack of a trade-off between b and d allows attenuation effects to be estimated independently. We assume $p = 3$ as the geometrical spreading term for body waves. We discarded data with a correlation coefficient between the theoretical model and experimental data obtained from the fit lower than 0.7 ($R < 0.7$). Finally, we used b and d in equations (3) and (4) to obtain Q_i and Q_s . Given b and d , the transport mean free path ($l_{tr} = 3d/v$) and the absorption length ($l_i = v/b$) can also be calculated. Figure 2b shows two examples of best fits.

2.4. Mapping Spatial Variation of Attenuation

To compute the spatial distribution of intrinsic and scattering attenuations we followed the back projection method described by Del Pezzo et al. (2016) based on a space weighting function obtained through numerical simulation of the transport equation. In the present paper we briefly describe the weighting method and the imaging technique, and for more detailed information the reader is referred to Del Pezzo et al. (2016).

1. Following Yoshimoto (2000), energy envelopes were numerically estimated using numerical simulations with the Monte Carlo technique. In this approach the seismic energy particles propagate following Fermat's rules and change their direction when they encounter a scatterer (the scatterers are assumed to be randomly distributed, with the shape of their distribution depending on the attenuation parameters). The sum of their energies at the receiver, as a function of propagation time, defines the energy envelope.
2. There are two separate weighting functions, one for intrinsic attenuation and a second for scattering attenuation. The one for intrinsic attenuation is obtained from the path density (the number of elementary paths inside a small volume), while the scattering attenuation function was obtained from the collision density (the number of scatterers that produced the synthetic envelope). In case diffusion occurs, it has been observed that the two weighting functions have almost the same shape and for that reason we applied a unique weighting function for both intrinsic and scattering attenuation imaging. This weighting function is characterized by two peaks located at the position of the receiver and source.
3. For each event-station pair, Q_i and Q_s space distributions can be expressed as the product of the weighting function described above. We divided the area into 5×5 -km² cells, corresponding to the highest resolution obtained from the synthetic tests, and in each cell we assigned the corresponding Q_i and Q_s values using the two-peaked weighting procedure based on each event-station pair. The final spatial distributions of the intrinsic and scattering attenuations were obtained by averaging all Q_i and Q_s values assigned to every cell.

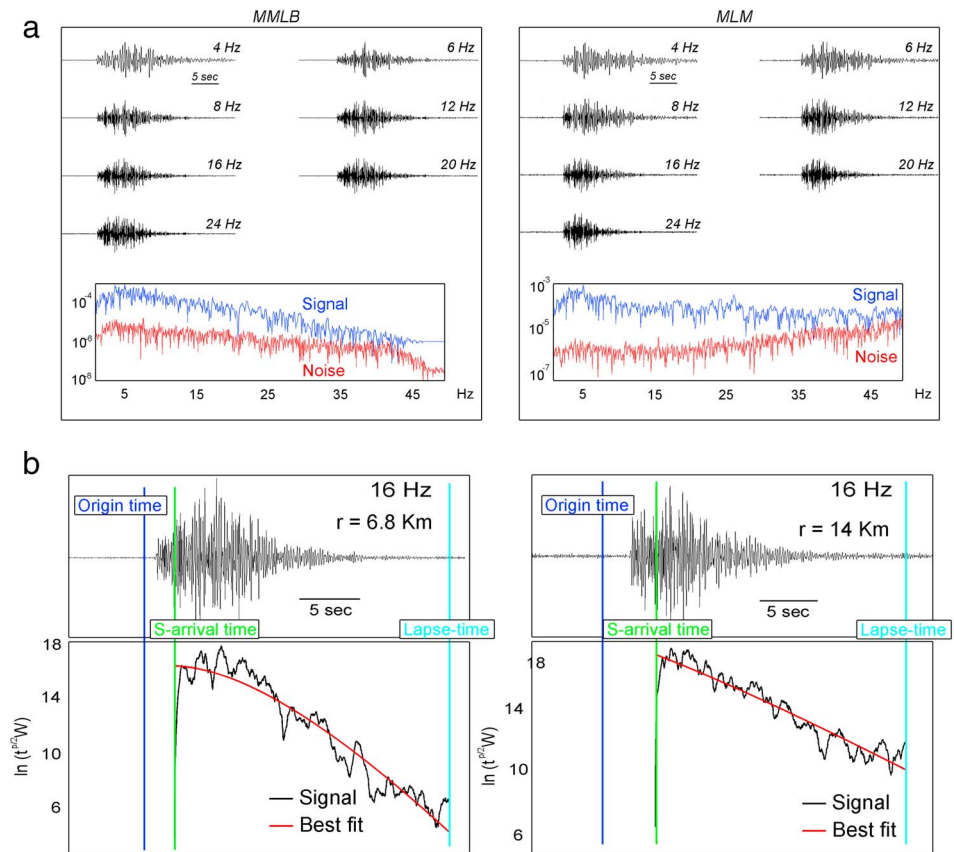


Figure 2. (a) Vertical records of earthquake 71748030 recorded at stations MLM and MMLB for the seven frequency bands with corner frequencies at $0.4f_c$ and $1.6f_c$ analyzed and their unfiltered spectra. Signal spectrum is plotted with blue color and obtained by analyzing 1-s time window after P -wave arrival time. Noise spectrum is plotted with a red line, and it corresponds to 1-s time window 5 s before P -wave arrival time. (b) Two examples of the best fit of observed energy envelope (black line) at 16 Hz and theoretical curve (red line) for the logarithmic energy density corrected for geometrical spreading of body waves as a function of time.

2.5. Synthetic Tests

We performed a checkerboard test to assess the resolution of the representation method. This synthetic test only evaluates the maximum resolution we can reach with the current source-station coverage, with the attenuation values already obtained from fitting the diffusion model to the data.

We assign different input values of b and d to each cell, with $b = 0.4$ ($Q_i = 100$) and $d = 7$ ($Q_s = 352$) for low anomalies and $b = 0.75$ ($Q_i = 50$) and $d = 0.06$ ($Q_s = 3$) for high anomalies. For i th source-receiver couple we estimated average b and d parameters (b_i and d_i , which correspond to i th couple) weighted by the same probability function used. Finally, we obtained the reconstructed images (d, e, and f panels in Figures 3 and 4). The results show that the selected cell dimension ($5 \times 5 \text{ km}^2$) should allow us to interpret the distribution of intrinsic and scattering attenuations in Long Valley Caldera.

3. Results and Discussion

There is a long history of developing rock physics models to relate rock properties to seismic attenuation (e.g., Biot, 1956; Mavko & Nur, 1979; Mavko, 1980; O'Connell & Budiansky, 1977; White, 1975; Winkler & Nur, 1979). An outstanding challenge remains, however, to address issues of scale and to relate rock physics models to both scattering and intrinsic Q . For these reasons, geological interpretation of attenuation images remains mostly based on qualitative considerations founded on the understanding of how rock physics properties should influence attenuation.

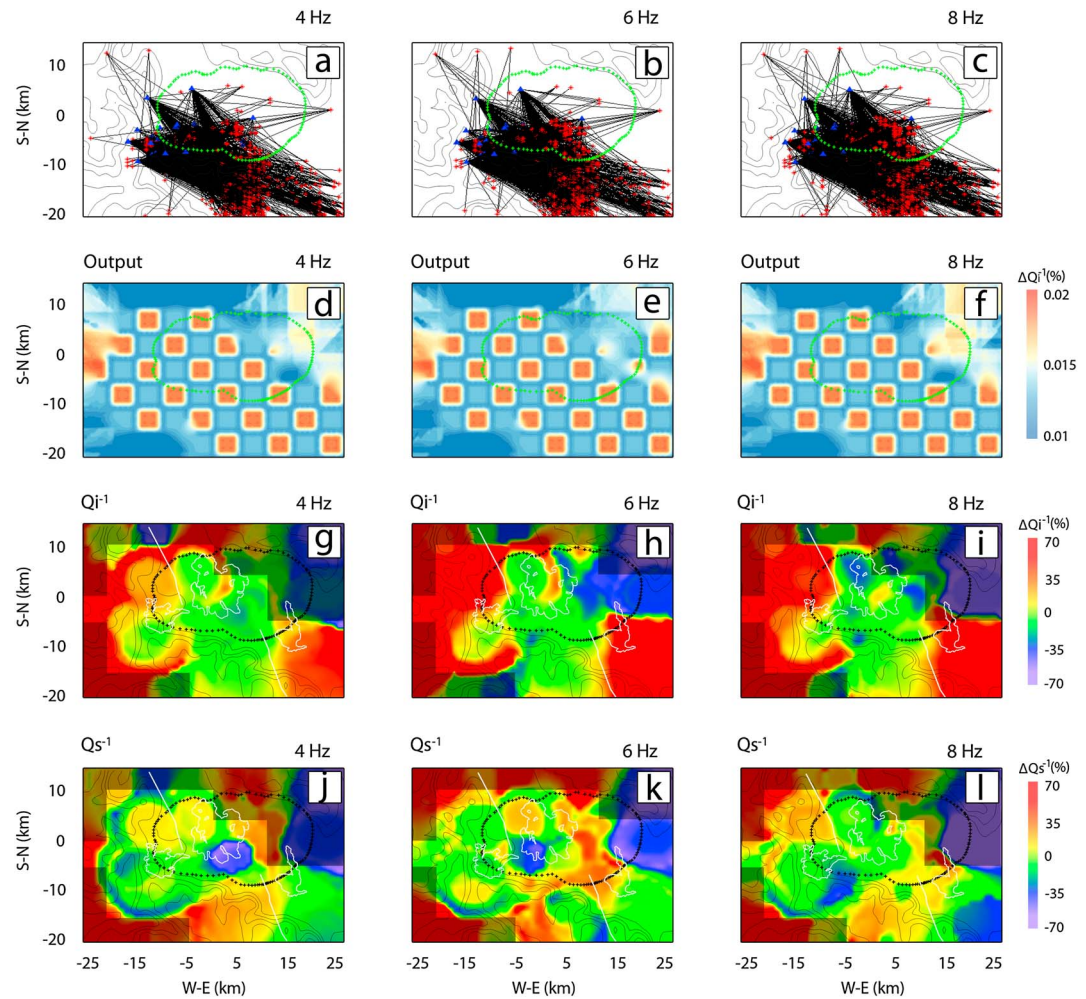


Figure 3. Ray paths, checkerboard test output images, and Q_i^{-1} and Q_s^{-1} distribution for 4-, 6-, and 8-Hz central frequencies. (a–c) Ray paths. (d–f) Checkerboard tests with $5 \times 5\text{-km}^2$ cell size. We respectively assigned $b = 0.75$ ($Q_i = 50$) and $d = 0.21$ ($Q_s = 3$) for the high intrinsic and scattering anomalies and $b = 0.4$ ($Q_i = 100$) and $d = 23$ ($Q_s = 333$) for the low anomalies. (g–i) Q_i^{-1} distribution. (j–l) Q_s^{-1} distribution.

3.1. Topographic Effects, Depth Dependence, and “Leakage Effect” of Attenuation Parameters

The interpretation of attenuation parameters is complicated by depth and “leakage” effects and topography, all of which can be important in volcanic areas.

Most volcanoes are characterized by large relief that is one of the main sources of surface wave scattering (Bean et al., 2008; Del Pezzo et al., 1997; Lokmer & Bean, 2010; O’Brien & Bean, 2004, 2009). However, Lokmer and Bean (2010) concluded that long-time coda remains unaffected, while only the early coda is modified by topography. We cannot exclude topographic effects from our interpretations, but we are confident that these effects are minor, especially when we image attenuation anomalies.

Attenuation parameters and their depth dependence have been widely studied and reported in the literature (e.g., Bianco et al., 2005; Del Pezzo et al., 1995; Ibañez et al., 1990). The main conclusion of these examples is that depth dependence of seismic attenuation exists and it becomes stronger when the distance between the earthquake and station is larger, in most cases larger than 200 km. The coda window analyzed here corresponds to the first 30 s of the seismogram and, as demonstrated by previous authors, early parts of coda waves are less sensitive to the depth dependence of attenuation. At the shallow 3- to 5-km depths that dominate our attenuation imaging, seismic tomography images reveal large lateral variations (Lin, 2015); hence, depth dependence will have less significant effects on the anomaly pattern.

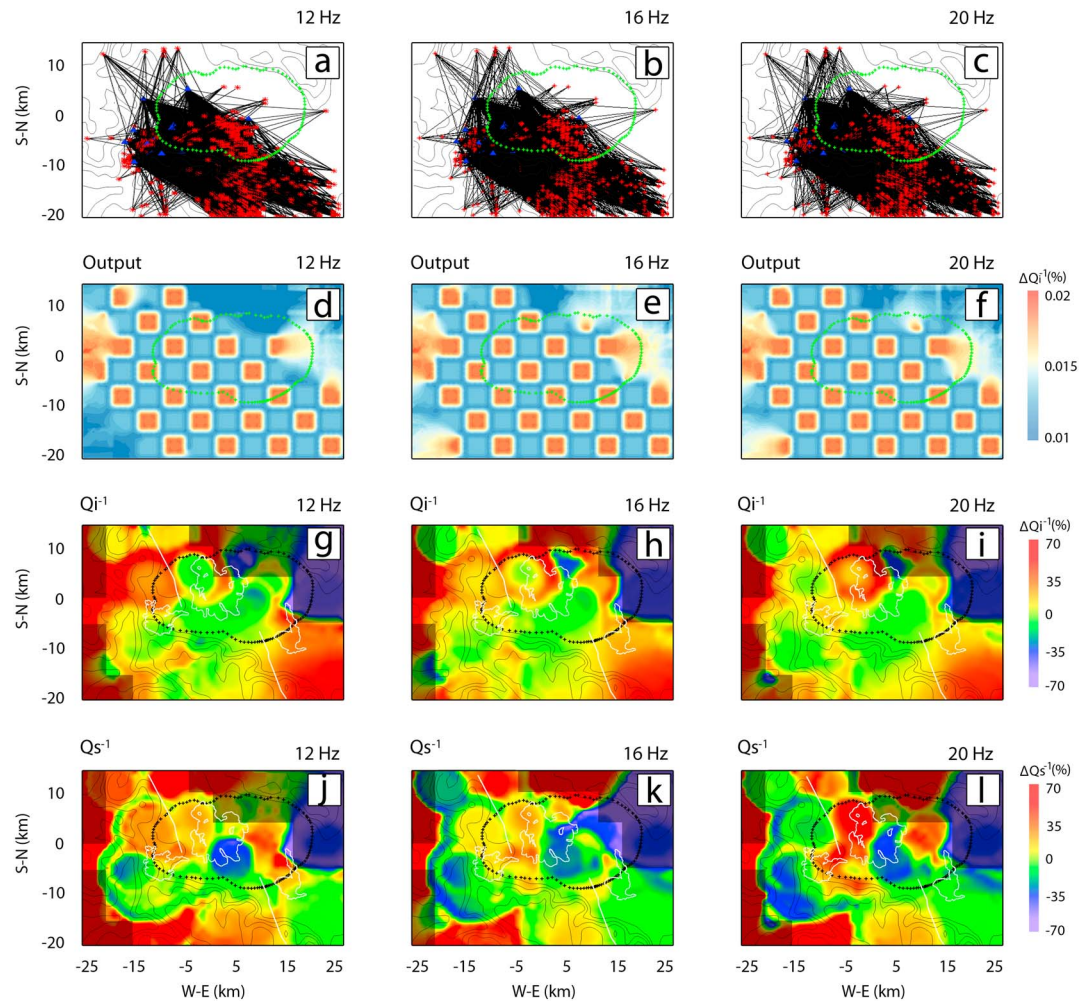


Figure 4. Ray paths, checkerboard test output images, and Q_i^{-1} and Q_s^{-1} distribution for 12-, 16-, and 20-Hz central frequencies. (a–c) Ray paths. (d–f) Checkerboard tests with $5 \times 5\text{-km}^2$ cell size. We respectively assigned $b = 0.75$ ($Q_i = 50$) and $d = 0.21$ ($Q_s = 3$) for the high intrinsic and scattering anomalies and $b = 0.4$ ($Q_i = 100$) and $d = 23$ ($Q_s = 333$) for the low anomalies. (g–i) Q_i^{-1} distribution. (j–l) Q_s^{-1} distribution.

Together with topography and depth dependent effects, the leakage effect may also introduce bias in intrinsic attenuation measurements (Margerin et al., 1998; Wegler, 2004) when measuring coda Q . Margerin et al. (1998) explained leakage for long coda from the transmission of energy in the mantle (with seismic scattering contribution absent) with no return into the coda. Wegler (2004) showed that when scattering occurs in a thin layer overlying a transparent half space, energy leakage is higher. In velocity tomography images, electrical resistivity models, and attenuation images there are strong lateral variations (high heterogeneity). Therefore, leakage effect due to the structure described by Wegler (2004), of a thin layer overlying a transparent half space, can be disregarded. If some leakage exists, absolute values of the estimated parameters could be affected while the pattern of spatial variations will remain the same.

3.2. Intrinsic and Scattering Attenuation Distribution in Long Valley Caldera

Table 1 summarizes average values of Q_i , Q_s , Q_{tr} , l_{tr} , and l_i for each central frequency estimated by fitting the diffusion model to the energy envelopes. Long Valley Caldera results are in agreement with the values obtained in other volcanic areas in that scattering phenomena dominate over intrinsic attenuation (Prudencio et al., 2017, and references therein). The average values for Long Valley are similar to those obtained for Stromboli Island ($l_{tr} \approx 200$ m and $l_i \approx 20$ km; Prudencio et al., 2015) and Deception Island ($l_{tr} \approx 950$ m and $l_i \approx 5$ km; Prudencio et al., 2013) and may allow us to confirm the presence of strong geological heterogeneities from geothermal systems and shallow melted material.

Table 1
Average Values of Q_i , Q_s , Q_t , l_{tr} , and l_i for Long Valley Caldera

Hz	Q_i^{-1}	Q_s^{-1}	Q_t^{-1}	Q_i	Q_s	Q_t	l_{tr} (m)	l_i (km)
4	0.0085 ± 0.0004	0.25 ± 0.05	0.26 ± 0.03	117	4	4	500	15
6	0.0078 ± 0.0006	0.20 ± 0.01	0.21 ± 0.02	128	5	5	445	12
8	0.0067 ± 0.0006	0.20 ± 0.01	0.21 ± 0.02	148	5	5	320	7
12	0.0056 ± 0.0004	0.16 ± 0.02	0.17 ± 0.02	180	6	6	290	5
16	0.0049 ± 0.0005	0.14 ± 0.02	0.14 ± 0.03	201	7	7	220	5
20	0.0043 ± 0.0003	0.12 ± 0.03	0.12 ± 0.03	230	8	8	230	5
24	0.0038 ± 0.0002	0.11 ± 0.003	0.11 ± 0.03	260	9	9	210	4

The intrinsic and scattering anomaly distributions estimated with respect to the average values in Table 1 are presented in Figures 3–5. Because intrinsic attenuation is at least 1 order of magnitude lower than scattering attenuation, total attenuation perturbations are dominated by scattering attenuation and therefore total attenuation images are not shown.

Attenuation images are an average over the first 3–5 km below Long Valley Caldera. We estimated this depth by assuming a depth equal to the minor axis of the scattering ellipsoid and the observed ray coverage. We obtained the maximum ray coverage between 3- and 5-km depths. It is thus likely that the structure we observe is dominated by the volume between these depths.

The spatial distributions of intrinsic and scattering anomalies, while not identical, are similar in all frequency bands analyzed. Lateral variations are up to 70% with respect to the average values in Table 1.

HSF (western edge of the caldera) shows different intrinsic and scattering behavior on both sides of the fault, and the trace of the fault can be easily identified (Anomaly A1). HCF (southeast of the caldera), in contrast, does not show this behavior. We found average to high attenuation values at Mammoth Mountain (southwest of the caldera, Anomaly A2). Finally, a marked low attenuation anomaly is observed in the center of the caldera, coincident with the position of the southeastern side of the resurgent dome (Anomaly A3). All these anomalies are superimposed in Figure 5 and will be discussed in the following sections.

3.3. Anomaly A1: HSF

While HCF (in Figure 5) is not easily identified, HSF (in Figure 5) is recognized in both intrinsic and scattering attenuation images. At lower frequencies (4 and 6 Hz) the western side (West in Figure 5), corresponding to Sierra Nevada block, shows higher attenuation than the eastern side (East in Figure 5). However, this behavior is the opposite at higher frequencies (20 and 24 Hz): The western side shows lower attenuation and the eastern side higher attenuation and is consistent in both intrinsic and scattering images. To check whether this opposite behavior is due to the increasing average value of the region or due to a change in lithologies, we estimate the average values of each side at all frequency bands analyzed. The average values are shown in Figure 6. As can be observed, the eastern side of the fault (East) has a similar average value at all frequencies. In contrast, on the western side (West) attenuation varies with frequency, ranging from high attenuation (at low frequencies) to low attenuation (at high frequencies). Following standard wave propagation theory, the high attenuation at deeper depths (low frequencies) on the West side of the fault may reflect the higher heat flow and warmer temperatures produced by the magmatic system that produced the Inyo Craters and, consequently, a more homogeneous and consolidated structure on the East. However, associating depth and frequency is not straightforward for our images because weighting function are more sensitive to structure around the source and station (Del Pezzo et al., 2016). In addition, secondary sources will activate when primary wavefront passes through heterogeneities, and the frequency sensitivity will be also related with the size of the heterogeneities (Yamamoto & Sato, 2010). We may thus interpret the western side of HSF as more heterogeneous (any heterogeneity and of any size), which may be related to old structures or signatures produced during the Inyo eruptions, whereas the eastern side is more homogeneous. It is possible that this interpretation is not unique and further imaging, analysis, and geological studies are needed to confirm (or not) that the frequency dependency of attenuation values observed on the western side corresponds to remaining heat and structures produced by Inyo Crater eruptions.

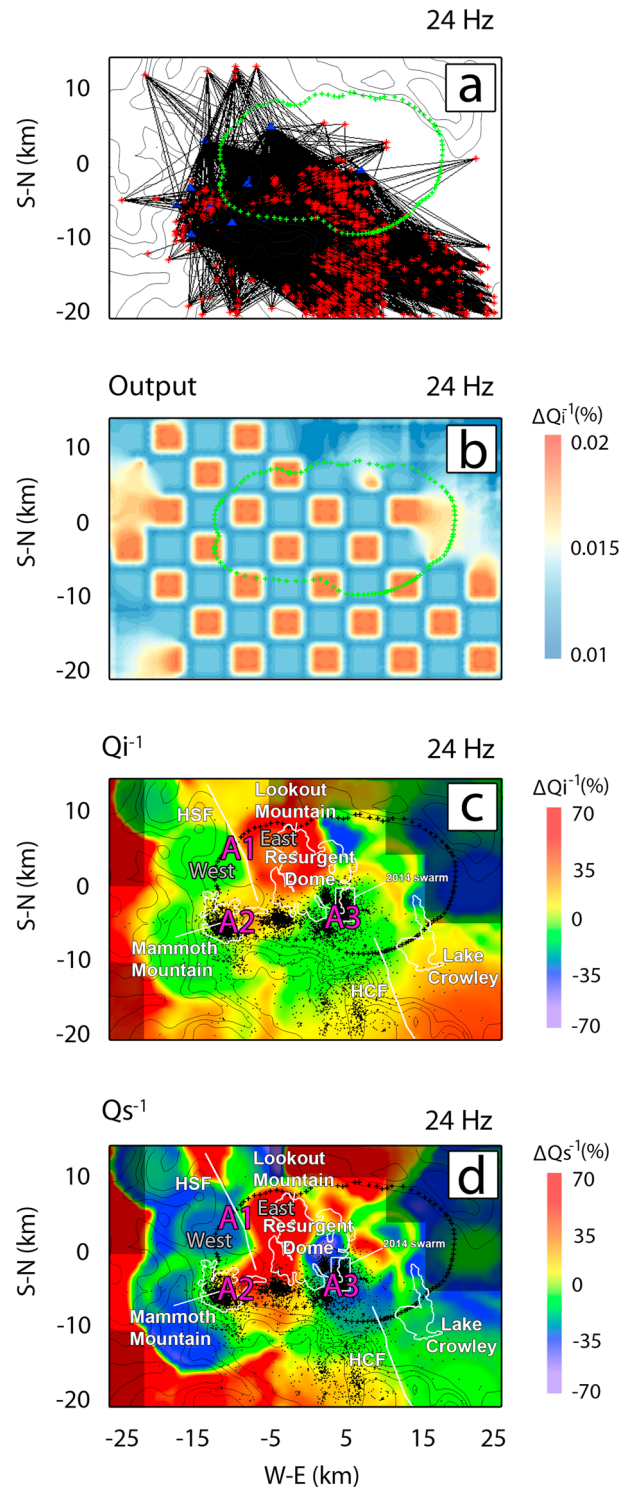


Figure 5. Ray paths, checkerboard test output images, and Q_i^{-1} and Q_s^{-1} distribution for 24-Hz central frequency. (a–c) Ray paths. (d–f) Checkerboard tests with $5 \times 5 \text{ km}^2$ cell size. We respectively assigned $b = 0.75$ ($Q_i = 50$) and $d = 0.21$ ($Q_s = 3$) for the high intrinsic and scattering anomalies and $b = 0.4$ ($Q_i = 100$) and $d = 23$ ($Q_s = 333$) for the low anomalies. (g–i) Q_i^{-1} distribution. (j–l) Q_s^{-1} distribution. Main geologic features and 2014 earthquakes are superimposed in Q_i^{-1} and Q_s^{-1} images. The 2014 earthquake swarm below the southeast edge of the resurgent dome (Shelly et al., 2015) is included in a white square. A1–A3 correspond to the anomalies discussed in the text. West and East labels correspond to each side of the fault discussed in the text. HSF = Hartely Springs Fault; HCF = Hilton Creek Fault.

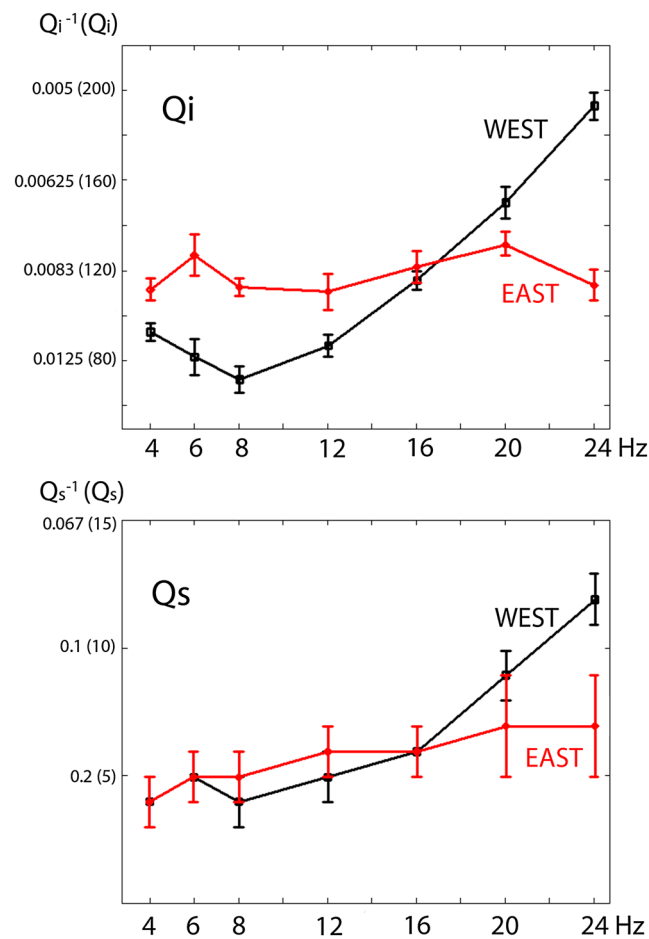


Figure 6. Average values at each frequency band analyzed for the western (WEST) and eastern (EAST) side of Hartley Springs Fault. Upper panel correspond to intrinsic attenuation average values and bottom panel to scattering attenuation.

3.4. Anomaly A2: Mammoth Mountain

Average to high intrinsic and scattering attenuation values are observed at Mammoth Mountain, southwest of the caldera. Sanders (1993) and Ponko and Sanders (1994) image an area of high P -wave attenuation at 4–5 km beneath the east side of Mammoth Mountain, which they interpreted as a region of fractured rock with supercritical hydrothermal fluids. More recently, Peacock et al. (2016) also inferred a shallow isolated hydrothermal system in their magnetotelluric (MT) images, which extends to around 3-km depth below the northeastern part of Mammoth Mountain (C4 in Figure 3 in Peacock et al., 2016). This anomaly is also coincident with a lower P -wave velocity (Foulger et al., 2003; Lin, 2013; Seccia et al., 2011) and average V_p/V_s ratio (Dawson et al., 2016; Foulger et al., 2003; Lin, 2013, 2015). Magmatic CO_2 gas emissions in the same area testify to the system being active (Lewicki et al., 2014, 1998). Based on these complementary studies, average to high attenuation values may correspond to hot and heterogeneous materials and fluids and we attribute this anomaly to have a hydrothermal origin.

3.5. Anomaly A3: Resurgent Dome

We observe low intrinsic and very low scattering attenuation anomalies in the center-southeast of the resurgent dome. This anomaly is located in the same area as the 2014 earthquake swarm, the largest swarm in the caldera since the 1997–1998 swarms (Shelly et al., 2015; black dots inside the white square in Figure 5). Kissling (1988) and Foulger et al. (2003) found lower P -wave velocities in the same region between 3- and 7-km depths. Our low attenuation anomaly is roughly collocated with a high P -wave velocity (Lin, 2015; Seccia et al., 2011) and a resistive body found by Peacock et al. (2016). In the same region, Prejean et al. (2002) attributed ascending earthquake swarms to fluids rising from deeper depths. Furthermore, studies of well Long Valley Exploratory Well (LVEW) and springs close to the resurgent dome found present-day deep tem-

peratures as low as 100 °C and mineral deposits precipitated by hydrothermal systems (Farrar et al., 2003; Sorely et al., 1991). Low intrinsic and very low scattering anomalies can be attributed to homogeneous consolidated and/or cooled bodies (De Lorenzo et al., 2001), and therefore, this body may be interpreted as a hydrothermally altered body. The region shows low attenuation (consolidated and homogeneous) because fractures have been filled.

4. Conclusions

We use a diffusion model to separately estimate intrinsic and scattering seismic attenuation coefficients of Long Valley Caldera using a data set composed by more than 1,700 vertical waveforms for the lowest frequency (4 Hz) and up to 22,000 for the highest frequency (24 Hz). A space weighting function is applied to image their spatial distribution. Checkerboard tests demonstrate the robustness and stability of the method and confirm that the obtained anomalies are reproducible with the cell size we use. The regional distributions of intrinsic and scattering attenuation anomalies do not vary with frequency, indicating that the results are not a mathematical artifact but image real structures.

The images support the conclusions by other authors that there is a shallow hydrothermal system at Mammoth Mountain. We interpret the low intrinsic and very low scattering anomalies observed at the location of the resurgent dome and the location of 2014 earthquake swarm as mapping a hydrothermally altered body in which fractures have been filled. We find no anomalies in the upper 8 km of the crust that we can conclusively attribute to melt. Finally, we image HSF and find that both intrinsic and scattering attenuations are different on each side of the fault.

Acknowledgments

Comments from two anonymous reviewers and editor significantly improve the manuscript. Waveform data for this study were accessed through the Northern California Earthquake Data Center (NCEDC), doi:10.7932/NCEDC. J. P. and M. M. are supported by the NSF-1521855 Hazard SEES project. J. P. is partially granted by Spanish KNOWAVES (TEC2015-68752) project. The numerical data behind the figures and attenuation models can be found in Prudencio et al. (2018), doi:10.6078/D1M08W.

References

- Bailey, R. A., Dalrymple, G. B., & Lanphere, M. A. (1976). Volcanism, structure, and geochronology of Long Valley Caldera, Mono County, California. *Journal of Geophysical Research*, *81*(5), 725–744.
- Battaglia, M., Segall, P., Murray, J., Cervelli, P., & Langbein, J. (2003). The mechanics of unrest at Long Valley caldera, California: 1. Modeling the geometry of the source using GPS, leveling and two-color EDM data. *Journal of Volcanology and Geothermal Research*, *127*(3), 195–217.
- Battaglia, M., Segall, P., & Roberts, C. (2003). The mechanics of unrest at Long Valley caldera, California. 2. Constraining the nature of the source using geodetic and micro-gravity data. *Journal of Volcanology and Geothermal Research*, *127*(3), 219–245.
- Bean, C. J., Lokmer, I., & O'Brien, G. S. (2008). Influence of near-surface volcanic structure on long-period seismic signals and on moment tensor inversions: Simulated examples from Mount Etna. *Journal of Geophysical Research*, *113*, B08308. <https://doi.org/10.1029/2007JB005468>
- Bergfeld, D., Evans, W. C., Howle, J. F., & Farrar, C. D. (2006). Carbon dioxide emissions from vegetation-kill zones around the resurgent dome of Long Valley caldera, eastern California, USA. *Journal of Volcanology and Geothermal Research*, *152*(2006), 140–156.
- Bianco, F., del Pezzo, E., Malagnini, L., di Luccio, F., & Akinci, A. (2005). Separation of depth-dependent intrinsic and scattering attenuation in the northeastern sector of the Italian Peninsula. *Geophysical Journal International*, *161*(1), 130–142.
- Biot, M. A. (1956). Theory of propagation of elastic waves in a fluid-saturated porous solid. II. High frequency range. *Journal of Acoustic Society of America*, *28*, 179–181.
- Biot, M. A. (1956). Theory of propagation of elastic waves in a fluid-saturated porous solid. II. Low frequency range. *Journal of Acoustic Society of America*, 169–178.
- Black, R. A., Deemer, S. J., & Smithson, S. B. (1991). Seismic reflection studies in Long Valley Caldera, California. *Journal of Geophysical Research*, *96*, 4289–4300.
- Dainty, A. M., & Toksöz, M. N. (1981). Seismic codas on the Earth and the Moon: A comparison. *Physics of the Earth and Planetary Interiors*, *26*, 250–260.
- Dawson, P., Chouet, B., & Pitt, A. (2016). Tomographic image of a seismically active volcano: Mammoth Mountain, California. *Journal of Geophysical Research: Solid Earth*, *121*, 114–133. <https://doi.org/10.1002/2015JB012537>
- De Lorenzo, S., Gasparini, P., Mongelli, F., & Zollo, A. (2001). Thermal state of the Campi Flegrei caldera inferred from seismic attenuation tomography. *Journal of Geodynamics*, *32*, 467–486.
- De Siena, L., Thomas, C., Waite, G. P., Moran, S. C., & Klemme, S. (2014). Attenuation and scattering tomography of the deep plumbing system of Mount St. Helens. *Journal of Geophysical Research: Solid Earth*, *118*, 8223–8238. <https://doi.org/10.1002/2014JB011372>
- Del Pezzo, E. (2008). Seismic wave scattering in volcanoes. *Advances in Geophysics*, *50*, 353–371.
- Del Pezzo, E., Bianco, F., & Zaccarelli, L. (2006). Separation of Q_i and Q_s from passive data at Mt. Vesuvius: A reappraisal of the seismic attenuation estimates. *Physics of the Earth and Planetary Interiors*, *159*, 202–212.
- Del Pezzo, E., Ibáñez, J. M., Morales, J., Akinci, A., & Maresca, R. (1995). Measurements of intrinsic and scattering seismic attenuation in the crust. *Bulletin of Seismological Society of America*, *85*, 1373–1385.
- Del Pezzo, E., Ibáñez, J., Prudencio, J., Bianco, F., & De Siena, L. (2016). Absorption and scattering 2-D volcano images from numerically calculated space-weighting functions. *Geophysical Journal International*, *206*(2), 742–756.
- Del Pezzo, E., La Rocca, M., & Ibáñez, J. M. (1997). Observations of high-frequency scattered waves using dense array at Teide volcano. *Bulletin of Seismological Society of America*, *87*, 1637–1647.
- Dreger, D. S., Tkalčić, H., & Johnston, M. (2000). Dilational processes accompanying earthquakes in the Long Valley Caldera. *Science*, *288*, 122–125.
- Eichelberger, J. C., Lysne, P. C., & Younker, L. W. (1984). Research drilling at Inyo Dome, Long Valley Caldera, California. *Eos, Transactions American Geophysical Union*, *65*(721), 723–725.

- Farrar, C. D., Sorey, M. L., Roeloffs, E., Galloway, D. L., Howle, J. F., & Jacobson, R. (2003). Inferences on the hydrothermal system beneath the resurgent dome in Long Valley Caldera, east-central California, USA, from recent pumping tests and geochemical sampling. *Journal of Volcanology and Geothermal Research*, *127*(3), 305–328.
- Fink, J. H. (1985). The geometry of silicic dikes beneath the Inyo domes, California. *Journal of Geophysical Research*, *90*, 11,127–11,133.
- Foulger, G. R., Julian, B. R., Pitt, A. M., Hill, D. P., Malin, P. E., & Shalev, E. (2003). Three-dimensional crustal structure of Long Valley caldera, California, and evidence for the migration of CO₂ under Mammoth Mountain. *Journal of Geophysical Research*, *108*, 2147.
- Heumann, A., Davies, G. R., & Elliott, T. (2002). Crystallization history of rhyolites at Long Valley, California, inferred from combined U-series and Rb-Sr isotope systematics. *Geochimica et Cosmochimica Acta*, *66*, 1821–1837.
- Hildreth, W. (2004). Volcanological perspectives on Long Valley, Mammoth Mountain, and Mono Craters: Several contiguous but discrete systems. *Journal of Volcanology and Geothermal Research*, *136*, 169–198.
- Hildreth, W. (2017). Fluid-driven uplift at Long Valley Caldera, California: Geologic perspectives. *Journal of Volcanology and Geothermal Research*, *341*, 269–286.
- Hill, D. P. (1976). Structure of Long Valley caldera, California, from a seismic refraction experiment. *Journal of Geophysical Research*, *81*, 745–753.
- Hill, D. P. (2006). Unrest in Long Valley Caldera, California, 1978–2004. *Geological Society of London Special Publication*, *269*(1), 1–24.
- Hill, D. P., Ellsworth, W. L., Johnston, M. J. S., Langbein, J., Oppenheimer, D. H., Pitt, A., et al. (1990). The 1989 earthquake swarm beneath Mammoth Mountain, California: An initial look at the 4 May through 30 September activity. *Bulletin of Seismological Society of America*, *80*, 325–339.
- Hill, D. P., Langbein, J., & Prejean, S. (2003). Relations between seismicity and deformation during unrest in Long Valley Caldera, California, from 1995 through 1999. *Journal of Volcanology and Geothermal Research*, *127*(3), 175–193.
- Hill, D. P., & Prejean, S. (2005). Magmatic unrest beneath Mammoth Mountain, California. *Journal of Volcanology and Geothermal Research*, *146*, 257–283.
- Hurwitz, S., Christiansen, L. B., & Hsieh, P. A. (2007). Hydrothermal fluid flow and deformation in large calderas: Inferences from numerical simulations. *Journal of Geophysical Research*, *112*, B02206. <https://doi.org/10.1029/2006JB004689>
- Hurwitz, S., Farrar, C. D., & Williams, C. F. (2010). The thermal regime in the resurgent dome of Long Valley Caldera, California: Inferences from precision temperature logs in deep wells. *Journal of Volcanology and Geothermal Research*, *198*, 233–240.
- Hutnak, M., Hurwitz, S., Ingeritsen, S. E., & Hsieh, P. E. (2009). Numerical models of caldera formation: Effects of multiphase and multicomponent hydrothermal fluid flow. *Journal of Geophysical Research*, *114*, B04411. <https://doi.org/10.1029/2008JB006151>
- Ibañez, J., Del Pezzo, E., De Miguel, F., Herraiz, M., Alguacil, G., & Morales, J. (1990). Depth-dependent seismic attenuation in the Granada zone (Southern Spain). *Bulletin of Seismological Society of America*, *80*, 1232–1244.
- Kissling, E. (1988). Geotomography with local earthquake data. *Reviews of Geophysics*, *26*, 659–698.
- Langbein, J. (2003). Deformation of Long Valley Caldera, California: Inferences from measurements from 1988 to 2001. *Journal of Volcanology and Geothermal Research*, *127*(3), 247–267.
- Lewicki, J. L., Hillel, G. E., Shelly, D. R., King, J. C., McGeehin, J. P., Mangan, M., & Evans, W. C. (2014). Crustal migration of CO₂-rich magmatic fluids recorded by tree-ring radiocarbon and seismicity at Mammoth Mountain, CA, USA. *Earth and Planetary Science Letters*, *390*, 52–58.
- Lin, G. (2013). Seismic investigation of magmatic unrest beneath Mammoth Mountain, California, USA. *Geology*, *41*(8), 847–850.
- Lin, G. (2015). Seismic velocity structure and earthquake relocation for the magmatic system beneath Long Valley Caldera, eastern California. *Journal of Volcanology and Geothermal Research*, *296*, 19–30.
- Lokmer, I., & Bean, C. J. (2010). Properties of the near-field term and its effect on polarisation analysis and source locations of long-period (LP) and very-long-period (VLP) seismic events at volcanoes. *Journal of Volcanology and Geothermal Research*, *192*(1), 35–47.
- Lucic, G., Stix, J., & Wing, B. (2015). Structural controls on the emission of magmatic carbon dioxide gas, Long Valley Caldera, USA. *Journal of Geophysical Research: Solid Earth*, *120*, 2262–2278. <https://doi.org/10.1002/2014JB011760>
- Margerin, L., Campillo, M., & Van Tiggelen, B. (1998). Radiative transfer and diffusion of waves in a layered medium: New insight into coda q. *Geophysical Journal International*, *134*, 596–612.
- Martínez-Arevalo, C., Patané, D., Rietbrock, A., & Ibáñez, J. (2005). The intrusive process leading to the Mt. Etna 2001 flank eruption: Constraints from 3-D attenuation tomography. *Geophysical Research Letters*, *32*, L21309. <https://doi.org/10.1029/2005GL023736>
- Mavko, G. (1980). Velocity and attenuation in partially molten rocks. *Journal of Geophysical Research*, *85*, 5173–5189.
- Mavko, G., & Nur, A. (1979). Wave attenuation in partially saturated rocks. *Geophysics*, *44*, 161–178.
- Miller, C. D. (1985). Holocene eruptions at the Inyo Craters volcanic chain, California: Implications for possible eruptions in Long Valley caldera. *Geology*, *13*, 14–17.
- Montgomery-Brown, E. K., Wicks, C. W., Cervelli, P., Langbein, J., Svarc, J. L., Shelly, D. R., et al. (2015). Renewed inflation of Long Valley Caldera, California (2011 to 2014). *Geophysical Research Letters*, *42*, 5250–5257. <https://doi.org/10.1002/2015GL064338>
- NCEDC (2014). Northern California Earthquake Data Center. CA: UC Berkeley Seismological Laboratory. Dataset.
- Nakata, N., & Shelly, D. R. (2018). Imaging a crustal low velocity layer using reflected seismic waves from the 2014 earthquake swarm at Long Valley Caldera, California: The magmatic system roof? *Geophysical Research Letters*, *45*, 3481–3488. <https://doi.org/10.1029/2018GL077260>
- O'Brien, G. S., & Bean, C. J. (2004). A 3D discrete numerical elastic lattice method for seismic wave propagation in heterogeneous media with topography. *Geophysical Research Letters*, *31*, L14608. <https://doi.org/10.1029/2004GL020069>
- O'Brien, G. S., & Bean, C. J. (2009). Volcano topography, structure and intrinsic attenuation: Their relative influences on a simulated 3D visco-elastic wavefield. *Journal of Geothermal Research*, *193*, 122–136.
- O'Connell, R. J., & Budiansky, B. (1977). Viscoelastic properties of fluid-saturated cracked solids. *Journal of Geophysical Research*, *82*(36), 5719–5735.
- Peacock, J. R., Mangan, M. T., McPhee, D., & Wannamaker, P. E. (2016). Three-dimensional electrical resistivity model of the hydrothermal system in Long Valley Caldera, California, from magnetotellurics. *Geophysical Research Letters*, *43*, 7953–7962. <https://doi.org/10.1002/2016GL069263>
- Ponko, S. C., & Sanders, C. O. (1994). Inversion for P and S wave attenuation structure, Long Valley caldera, California. *Journal of Geophysical Research*, *99*, 2619–2635.
- Prejean, S., Ellsworth, W. L., Zoback, M., & Waldhauser, F. (2002). Fault structure and kinematics of the Long Valley Caldera region, California, revealed by high-accuracy earthquake hypocenters and focal mechanism stress inversions. *Journal of Geophysical Research*, *107*(B12), 2355.
- Prejean, S., Stork, A., Ellsworth, W. L., Hill, D. P., & Julian, B. (2003). High precision earthquake locations reveal seismogenic structure beneath Mammoth Mountain, California. *Geophysical Research Letters*, *30*(24), 2247.

- Prudencio, J., Del Pezzo, E., García-Yeguas, A., & Ibáñez, J. M. (2013). Spatial distribution of intrinsic and scattering seismic attenuation in active volcanic islands, I: Model and the case of Tenerife Island. *Geophysical Journal International*, *195*(3), 1942–1956. <https://doi.org/10.1093/gji/ggt361>
- Prudencio, J., Del Pezzo, E., Ibáñez, J. M., Giampiccolo, E., & Patané, D. (2015). Two-dimensional seismic attenuation images of Stromboli Island using active data. *Geophysical Research Letters*, *42*, 1717–1724. <https://doi.org/10.1002/2015GL063293>
- Prudencio, J., Ibáñez, J. M., Del Pezzo, E., Martí, J., García-Yeguas, A., & De Siena, L. (2015). 3D attenuation tomography of the volcanic island of Tenerife (Canary Islands). *Surveys in Geophysics*, *36*, 693–716. <https://doi.org/10.1007/s10712-015-9333-3>
- Prudencio, J., Ibáñez, J. M., García-Yeguas, A., & Del Pezzo, E. (2013). Spatial distribution of intrinsic and scattering seismic attenuation in active volcanic islands, II: Deception island images. *Geophysical Journal International*, *195*(3), 1957–1969. <https://doi.org/10.1093/gji/ggt360>
- Prudencio, J., Manga, M., & Taira, T. (2018). 2D attenuation model of Long Valley (CA). Berkeley, CA: UC Berkeley Dash, Dataset. <https://doi.org/10.6078/D1M08W>
- Prudencio, J., Taira, T., Aoki, Y., Aoyama, H., & Onizawa, S. (2017). Intrinsic and scattering attenuation images of Usu volcano, Japan. *Bulletin of Volcanology*, *79*, 29. <https://doi.org/10.1007/s00445-017-1117-9>
- Rundle, J. B., & Hill, D. P. (1988). The geophysics of a restless caldera—Long Valley, California. *Annual Review in Earth and Planetary Science*, *16*, 251–271.
- Sanders, C. O. (1993). Reanalysis of S-to-P amplitude ratios for gross attenuation structure, Long Valley caldera, California. *Journal of Geophysical Research*, *98*, 22,069–22,079.
- Sato, H., Fehler, M., & Maeda, T. (2012). *Seismic wave propagation and scattering in heterogeneous Earth* (2nd ed.). Berlin: Springer.
- Savage, J. C., Cockerham, R. S., Estrem, J. E., & Moore, L. R. (1987). Deformation near the Long Valley Caldera, eastern California, 1982–1986. *Journal of Geophysical Research*, *92*(B3), 2721–2746.
- Seccia, D., Chiarabba, C., DeGori, P., & Hill, D. P. (2011). Evidence for the contemporary magmatic system beneath Long Valley Caldera from local earthquake tomography and receiver function analysis. *Journal of Geophysical Research*, *116*, B12314. <https://doi.org/10.1029/2011JB008471>
- Shelly, D. R., Ellsworth, W. L., & Hill, D. P. (2015). Fluid-faulting evolution in high definition: Connecting fault structure and frequency-magnitude variations during the 2014 Long Valley Caldera, California, earthquake swarm. *Journal of Geophysical Research: Solid Earth*, *121*, 1776–1795. <https://doi.org/10.1002/2015JB012719>
- Shelly, D. R., Ellsworth, W. L., & Hill, D. P. (2016). Fluid-faulting evolution in high definition: Connecting fault structure and frequency-magnitude variations during the 2014 Long Valley Caldera, California, earthquake swarm. *Journal of Geophysical Research: Solid Earth*, *121*, 1776–1795. <https://doi.org/10.1002/2015JB012719>
- Shelly, D. R., & Hill, D. P. (2011). Migrating swarms of brittle-failure earthquakes in the lower crust beneath Mammoth Mountain, California. *Geophysical Research Letters*, *38*, L20307. <https://doi.org/10.1029/2011GL049336>
- Shelly, D. R., Taira, T., Prejean, S., Hill, D. P., & Dreger, D. S. (2015). Fluid-faulting interactions: Fracture-mesh and fault-valve behavior in the February 2014 Mammoth Mountain, California, earthquake swarm. *Geophysical Research Letters*, *42*, 5803–5812. <https://doi.org/10.1002/2015GL064325>
- Sorey, M. L., Evans, W. C., Kennedy, B. M., Farrar, C. D., Hainsworth, L. J., & Hausback, B. (1998). Carbon dioxide and helium emissions from a reservoir of magmatic gas beneath Mammoth Mountain, California. *Journal of Geophysical Research*, *103*(B7), 15,303–15,323.
- Sorey, M. L., Suemnicht, G. A., Sturchio, N. C., & Nordquist, G. A. (1991). New evidence on the hydrothermal system in Long Valley caldera, California, from wells, fluid sampling, electrical geophysics, and age determinations of hot-spring deposits. *Journal of Volcanology and Geothermal Research*, *48*(3), 229–263.
- Suemnicht, G. A., Kennedy, B. M., & Evans, W. C. (2015). Helium isotope systematics of Long Valley Caldera, California, *Proceedings, World Geothermal Congress 2015* (pp. 1–6). Melbourne, Australia.
- Taylor, G. C., & Bryant, W. A. (1980). Surface Rupture Associated with the Mammoth Lakes Earthquakes of 25 and 27 May, 1980. In *Mammoth Lakes, California Earthquakes of May 1980, Special Report 150* (pp. 49–59). Sacramento, CA: California Division of Mines and Geology.
- Tizzani, P., Battaglia, M., Zeni, G., Atzori, S., Bernardino, P., & Lanari, R. (2009). Uplift and magma intrusion at Long Valley caldera from InSAR and gravity measurements. *Geology*, *37*, 63–66.
- Wegler, U. (2004). Diffusion of seismic waves in a thick layer: Theory and application to Vesuvius volcano. *Journal of Geophysical Research*, *109*, B07303. <https://doi.org/10.1029/2004JB003048>
- Wegler, U., & Lühr, B. G. (2001). Scattering behavior at Merapi Volcano (Java) revealed from an active seismic experiment. *Geophysical Journal International*, *145*, 579–592.
- White, J. E. (1975). Computed seismic speeds and attenuation in rocks with partial gas saturation. *Geophysics*, *40*(2), 224–232.
- Winkler, K. W., & Nur, A. (1979). Pore fluids and seismic attenuation in rocks. *Geophysical Research Letters*, *6*, 1–4.
- Yamamoto, M., & Sato, H. (2010). Multiple scattering and mode conversion revealed by an active seismic experiment at Asama volcano, Japan. *Journal of Geophysical Research*, *115*, B07304. <https://doi.org/10.1029/2009JB007109>
- Yoshimoto, K. (2000). Monte Carlo simulation of seismogram envelopes in scattering media. *Journal of Geophysical Research*, *105*, 6153–6161.
- Zeng, Y. (1991). Compact solutions for multiple scattered wave energy in time domain. 1. Theory. *Bulletin of Seismological Society of America*, *81*, 1022–1029.